Characterisation of copper and stainless steel surfaces treated with laser ablation surface engineering

A.N. Hannah[1,2], P. Krkotić[3,4], R. Valizadeh[1], O.B. Malyshev[1], J. Mutch[1], D.J. Whitehead[5], M. Pont[3], J.M. O'Callaghan[4] and V. Dhanak[2]

[1]ASTeC, STFC Daresbury Laboratory, Warrington, WA4 4AD, UK

[2] Dept. of Physics and Stephenson Institute for Renewable Energy, University of Liverpool, Liverpool, L69 7ZF, UK

[3] ALBA Synchrotron - CELLS, Cerdanyola del Vallés, Barcelona, 08290 Spain

[4]CommSenseLab, UPC, Barcelona, 08034Spain

[5]Laser Processing Research Centre (LPRC), Department of Mechanical, Aerospace and Civil Engineering, University of Manchester, Manchester M13 9PL, UK

Abstract

In the past few years, it has been established that Laser Ablation Surface Engineering (LASE) is a very effective way of producing surfaces which have Secondary Electron Yields (SEY) < 1. This can be achieved with a variety of laser pulse durations from nano- to picoseconds. However, the features (i.e. moderately deep grooves and nano-particulates) that help to reduce the SEY can produce undesirable effects such as an increase in the RF surface resistance. In this paper we discuss the methods employed utilising the dielectric resonator technique to quantify the surface resistance of laser treated copper and stainless steel samples. The quantification is based on a non-destructive measurement of high-frequency losses on the conducting surface. It has been demonstrated that the LASE surface can be produced with SEY<1 and an RF surface resistance of only ~6% higher than that on untreated surfaces. Furthermore, a comparative study of electron stimulated desorption (ESD) between the LASE treated and untreated samples of copper and stainless steel is reported for H_2, CH_4, CO and CO_2. It has been shown that there are negligible differences in ESD between LASE treated and untreated stainless steel. It has been demonstrated that LASE-

treated copper samples have a considerable reduction in ESD as compared with untreated sample.

1. INTRODUCTION

High intensity positively charged particle accelerators such as the LHC [1], ILC [2], KEKB [3], DAΦNE [4] and RHIC [5] may produce two coupled effects: electron cloud (e-cloud) and beam induced electron multipactoring (BIEM) [6,7]. BIEM can cause an e-cloud build-up inducing an increase in beam instability, beam losses, emittance growth, vacuum pressure increase, a reduction in the beam lifetime, or an additional heat load on a cryogenic vacuum chamber [8]. It has been specifically highlighted in many scientific presentations [9] that the high luminosity upgrade for the LHC (known as HL-LHC) requires complete elimination of the electron cloud. This is only possible when the beam screen surface SEY is reduced, ideally to less than unity.

The BIEM process can be described as follows: initial electrons appear from residual gas ionisation by beam particles or photoelectron emission (PEE) from beam pipe walls via synchrotron radiation emitted by accelerated particles in the dipoles and quadrupoles. These primary electrons are accelerated in the electric field of the passing bunches and can acquire kinetic energies up to several hundreds of eV. In turn, upon colliding with the wall of the chamber, they can cause secondary electron emission (SEE). BIEM is triggered by resonant conditions generated by the electromagnetic field of the beam train. Although the primary photon-induced emission and gas ionisation could be a significant source of electrons, the electron-wall impact, with energies in the range of 100 to 300 eV, can significantly increase the electron density by several orders of magnitude over the primary electron density.

It has been shown both theoretically and experimentally [6] that the e-cloud density build-up depends on the secondary electron yield (SEY) function δ(E). To minimize the effects of e-cloud, the δ_{max} value should be below a certain threshold value, but in all cases $\delta_{max} < 1$ would be a sufficient condition [6,10]. Since the secondary electron yield is influenced by the wall material, surface chemistry, topography and electron energy, any deliberate mitigation mechanism is based on engineering the first three of these parameters. Ways of reducing the SEY include [8]:

(a) Choice of material with low SEY (for example, Cu has lower δ(E) than Al);

(b) Modifying surface geometry (e.g. making grooves) [6,11];

(c) Coating with low δ(E) materials (such as TiN [12], Non-Evaporable Getters (NEG) [13] and amorphous carbon (a-C) [14]);

(d) Coating with low δ(E) microstructure (eg.: copper black, gold black);

(e) Columnar rather than dense NEG [15,16];

(f) Various combinations of the above [8].

More recently it has been discovered that Laser Ablation Surface Engineering (LASE) could provide surfaces with secondary electron yield $\delta < 0.9$ [17,18,19,20]. The technique involved to achieve this requires rapid surface micro- and nano-restructuring at room temperature utilising a high-power pulsed laser at various wavelengths for the processing of aluminium, stainless steel and copper surfaces. The average laser energy fluence is above the ablation threshold of the substrates. The process of lowering the SEY by laser treating surfaces is the most promising solution as it is technically simple and cost effective. The influence of micro- and nanostructures induced by laser surface treatment in air of copper samples as function of various laser irradiation parameters such as peak power of laser, number of pulses per point (scan speed and repetition rate) and fluence, on the SEY has been discussed at length in our previous paper [19].

It has been widely proven that the ablation mechanism highly depends on pulse duration [21]. Indeed, for pulse duration longer than 50 ps the pulse duration is long enough to have a heat transfer from the excited electrons to the lattice due to electron-phonon coupling. It is a pure thermal ablation mechanism. The heat diffuses outside the irradiated volume and affects a large amount of material. Therefore, in addition to the optical ablation process a thermal ablation mechanism takes an increasing share in the range of hundreds of picoseconds. Moreover, for nanosecond pulses the end of the incoming pulse is partially absorbed by the plasma produced by the beginning of the same pulse; this so-called “shielding effect” contributes to decrease in the process efficiency. Thus, towards the nanosecond range the removal rate is high but there are extensive side effects such as burr, over thickness, delamination, uncontrolled roughness, chemical modifications, etc.

The depth of microstructure (grooves and superimposed nanoparticles) under pulse durations between 50 ps to tens of nanosecond can be between several microns to hundreds of microns. The presence of such features on the inner surface of the vacuum vessel will reduce the SEY to the desirable threshold but at the same time will increase the RF surface resistance which leads to undesirable effects such as [22,23,24,25]:

- Increase of beam energy spread
- Significant resistive heat loss of beam image current on vacuum chamber walls.

The effectiveness of LASE treated surfaces for the e-cloud and BIEM mitigation was demonstrated on LASE copper surfaces in experiments carried out on a section of the SPS at CERN [26]. LASE surfaces are now considered as a baseline solution for e-cloud mitigation in the Future Circular Collider (FCC) [27].

As a new technology for application to particle accelerators, LASE treated samples are undergoing various testing and optimisation to meet the various requirements of an accelerator vacuum chamber. Apart from keeping $\delta < 1$ the surfaces should have low outgassing, low particulate generation and low surface resistance. The results in this paper are primarily focused on the effect of surface texturing on the SEY threshold, electron simulated desorption (ESD) and induced increase of the RF surface resistance (R_s). The main characteristics of LASE treated copper and stainless steel surfaces are reported together.

2. EXPERIMENTAL

2.1 Production of periodic structure on copper and stainless steel

The laser used for this study is 1063 nm, 30 W average power, with a pulse duration of 150 ps to 2 ns at repetition rate of 40 to 600 kHz (50 to 500 μJ per pulse). This results in a fluence of 11 to 111 J·cm^{-2} for a spot diameter of 30 μm at 1/e^2 intensity (where e is the maximum intensity). For SEY and surface resistance studies, the laser beam had a Gaussian intensity profile ($M^2 < 1.3$). It was focused onto the OFHC copper/stainless steel (11.5 mm × 11.5 mm) surfaces using a flat-field scanning lens system equipped with a tele-centric F-theta lens. The laser beam was raster scanned over the surface of the samples at 40 mm/s in a line hatched (LH) pattern using a computer-controlled scanner system. Five sets of three samples were irradiated with each process parameters shown in Table 1.

The fluence reported in Table 1 is the flat top equivalent:

$$F = \frac{E}{2\pi r^2} = \frac{2E}{\pi\omega^2}, \tag{1}$$

where E is the single pulse energy (J), r and ω are the beam radius and diameter (cm), respectively. For a Gaussian beam, the beam radius is typically expressed by 1/e^2 definition, *i.e.*, the distance at which the optical intensity of the beam falls to 1/e^2 or 13.5% of its peak value. The single pulse energy is calculated as:

$$E = \frac{P}{f} \tag{2}$$

where P (Watt) is the average power of the laser beam measured by a power meter and f (Hz) is the frequency (also called repetition rate) of the laser.

For ESD measurement samples C1-C4 are Cu blank gaskets ∅48 mm, and sample SS1 and SS2 are 316LN stainless steel flanges DN40. Samples C1, C2 and SS1 were LASE treated with laser parameters shown in Table 1, while samples C3, C4 and SS2 were used as untreated reference samples. Figure 1 shows an image of the samples SS1, SS2, C1 and C3.

Table 1. Sample sets and LASE treatment parameters.

	Sample Set Number						
Sample set	**1**	**2**	**3**	**4**	**5**	**6**	**7**
Material	Cu	Cu	Cu (C2)	Cu (C1)	SS (SS1)	Cu (C3)	SS (SS2)
Wavelength (nm)	1063	1063	1063	1063	1063	-	-
Average Power (W)	30	20	20	30	30	-	-
Pulse Length (ns)	0.15	2	2	2	0.15	-	-
Frequency (kHz)	600	60	60	60	600	-	-
Pitch (µm)	10	50	10	10	10	-	-
Beam Size (µm)	30	30	30	30	30	-	-
Energy per Pulse (µJ)	50	500	333	500	50	-	-
Fluence ($J \cdot cm^{-2}$)	11	111	74	111	11	-	-
Speed (mm/s)	40	40	40	40	40	-	-
δ_{max}	2.2	-	-	-	-	2.11	2.47
δ_{max} ***at Eph= 1000 eV***		1.1	1.03	0.78	1.49		

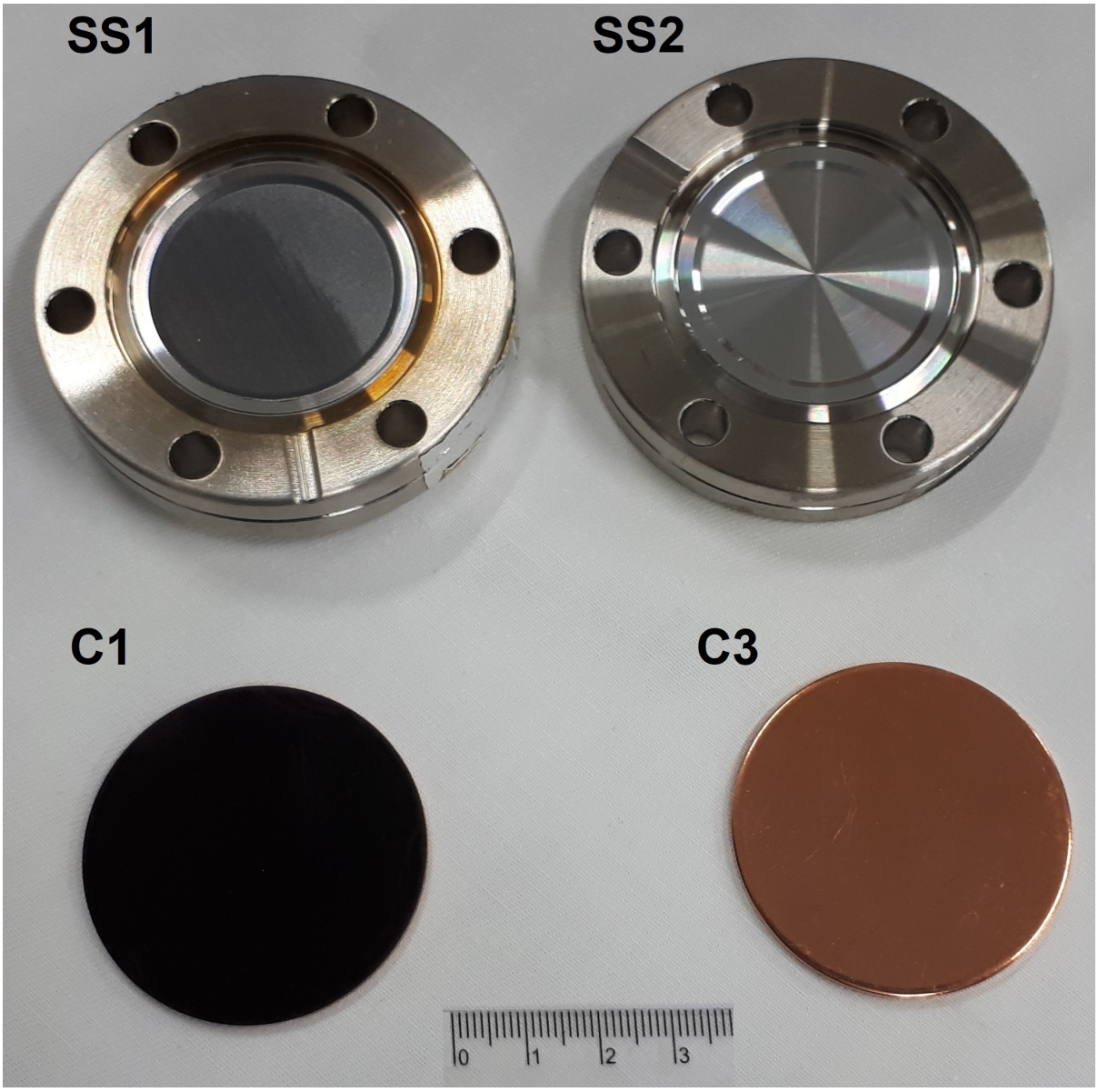

Figure 1. Samples: SS1 and C1 – LASE treated, SS2 and C3 untreated reference samples.

2.2 Facility for SEY and SEM studies

The facility consists of two chambers: a load-lock chamber and the SEY measurement chamber. The pressure of 2×10^{-9} mbar, measured using an MKS Pirani and inverted magnetron gauges, is routinely reached in both chambers after baking overnight for each set of sample batch introduced from atmosphere. The secondary electron yield (δ) was measured using an ELG-2 (0-2 keV) Kimball Physics Inc. electron gun. The measurement was performed using the configuration shown in Figure 2. I_p and I_s are the current registered on the gun Faraday cup and the sample (biased to –48 eV), respectively. The sample is then transferred into the UHV SEY measurement chamber. Before each measurement the primary electron current was

measured with both sample Faraday cup and the gun Faraday cup for each primary electron energy. The beam size at the sample (full width half maximum – FWHM) has been measured with a phosphor screen for different electron gun parameters and electron beam energies before performing the SEY experiments. The spot size during the SEY measurements was 0.28 cm^2.

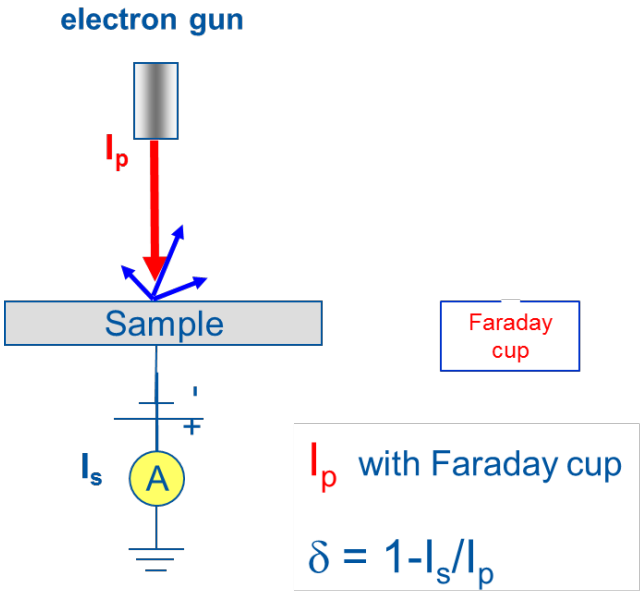

Figure 2. Schematic layout of the facility for SEY studies.

The surface topography and composition were examined using a high-resolution Hitachi Regulus 8230 scanning electron microscope (SEM) and the Bruker FlatQUAD energy dispersive x-ray (EDX), respectively.

2.3 Facility for ESD measurements

The layout of the facility for ESD measurements is shown in Figure 3. The test facility consists of a test chamber, pumping system and gas injection system.

The test chamber is equipped with an electron gun (EGG-3103A, Kimble), an XHV gauge (BARION, VACOM) and an RGA (Microvision 2, MKS).

The pumping system consists of a vacuum turbopump system (TURBOLAB80, Leybold) with pumping speed of 80 l/s (in N_2 eqv.), a sputter ion pump (SIP, TiTan DI, Gamma Vacuum) with pumping speed of S = 150 l/s (in N_2 eqv.) and a tube between the test chamber and SIP with a vacuum conductance U. The vacuum turbopump system is for the initial

pumping and for pumping during a bakeout of the test chamber whilst the sputter ion is for pumping during the ESD measurements.

The gas injecting system consists of a gas volume V_g and pressure P_g (measured with an MKS Baratron® high accuracy capacitance manometer), vacuum turbopump system and gas cylinders.

The gas injecting system is used for RGA calibration against the UHV gauge employing a procedure described in Ref. [28]. It was also used to measure an effective pumping speed (S_{eff}) at the test chamber. The injected gas flow can be calculated as:

$$Q = V_g \frac{dP_g}{dt} \approx V_g \frac{\Delta P_g}{\Delta t} \tag{3}$$

In the described facility, this method allows the measurement of gas flows in the range 10^{-8}–10^{-4} mbar·l/s. Then, S_{eff} can be measured for an injected gas i using partial pressure measurements P_i before (a) and during (b) gas injection:

$$S_i^{eff} = \frac{Q}{\left(P_{i,b} - P_{i,a}\right)} \tag{4}$$

The outgassing rate measurement from the test chamber employs an effective pumping speed method, where outgassing flow rate Q for each gas i can be calculated using a partial pressure P_i, a vacuum conductance U_i between the test chamber and pumps, and pumping speed S_i:

$$Q_i = P_i S_i^{eff} \tag{5}$$

This outgassing rate includes the TD from a sample. Considering that the sample area in this facility is a factor ~50 lower than the area of the test chamber, this facility is not suitable for measuring TD from such samples.

However, this system allows us to measure ESD yields. For this the partial pressures P_i are measured with and without electron bombardment, $P_i(I)$ and $P_i(I{=}0)$. Then the outgassing rate due to ESD can be calculated as:

$$\Delta Q_i = \left(P_i(I) - P_i(I=0)\right) S_i^{eff} = \Delta P_i S_i^{eff} \tag{6}$$

The ESD yield is defined as *a number of gas molecules desorbed from the surface per incident electron,* η [molecules/e$^-$] and can be calculated as:

$$\eta_i \left[\frac{molecules}{e^-}\right] = \frac{\Delta Q_i \left[Pa \cdot m^3/s\right] q_e [C]}{k_B T[K] I[A]} = \frac{\Delta P_i [Pa] S_i^{eff} \left[m^3/s\right] q_e [C]}{k_B T[K] I[A]}, \tag{7}$$

where k_B is the Boltzmann constant, q_e is the elementary charge, T is the gas temperature and I is the electron beam current.

The samples series C1-C4, S1 and S2 that were studied in this facility followed the same procedure. After mounting a sample at its location in the facility, the facility was pumped down and then baked to 200 °C for 24 hours. At the end of bakeout, when the test chamber was cooled to about 150 °C, the electron gun, UHV gauge and RGA were switched on and degassed. The ESD measurements were started 12 hours after reaching room temperature.

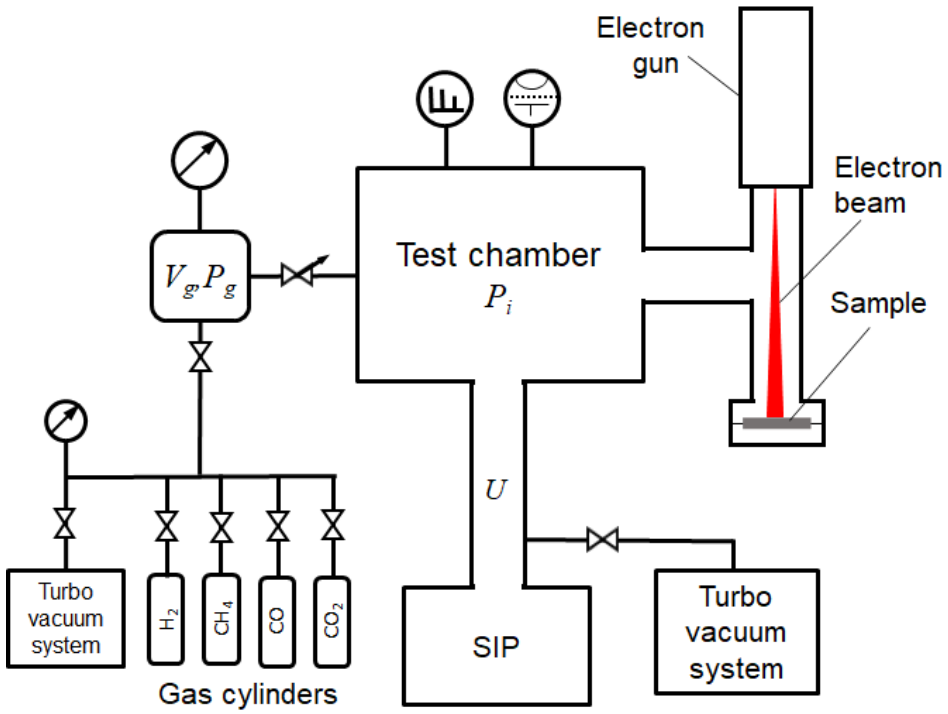

Figure 3. ESD measurement facility.

2.4 Facility for RF surface resistance measurements

The dielectric resonator (DR) used for this study is composed of a closed metallic body housing a small dielectric rutile (TiO_2) cylinder shielded axially by the two laser treated copper samples to be measured. The resonating structure sketched in Figure 4(a) is supported by two copper-beryllium springs to avoid a shifting of the dielectric rod inside the resonator and to close the resonating structure. The inductive coupling is achieved through the lateral walls by a pair of semi-rigid coaxial cables with a loop at each end. It is possible to adjust the coupling by changing the insertion depth of the cables. The resonant frequency of the cavity is

determined by its physical dimensions as well as on the size and permittivity of the dielectric used. A polished c-axis oriented high-purity rutile TiO_2 dielectric cylinder was used, with dielectric properties that show low tangential loss and high permittivity, ranging from $\varepsilon_r = 86$ to 110 F/m. Thus, for samples sizes of 12 mm × 12 mm, this results in a resonance frequency of between 7.9–9.1 GHz in the TE_{011} mode at room temperature and cryogenic temperature, respectively. The benefit of using this mode lies within the insensitivity of the electrical contact between the samples and lateral wall. The field distribution of this mode results in circular surface currents that are mainly focused in the centre of the sample at the edges of the dielectric rod, as can be seen in Figure 4(b). Several materials have already been successfully measured with this device; metal plates and coatings deposited on plastic [29], graphene [30], as well as high-temperature superconductors [31]. For a more detailed description of the resonator, see Refs. [29,30].

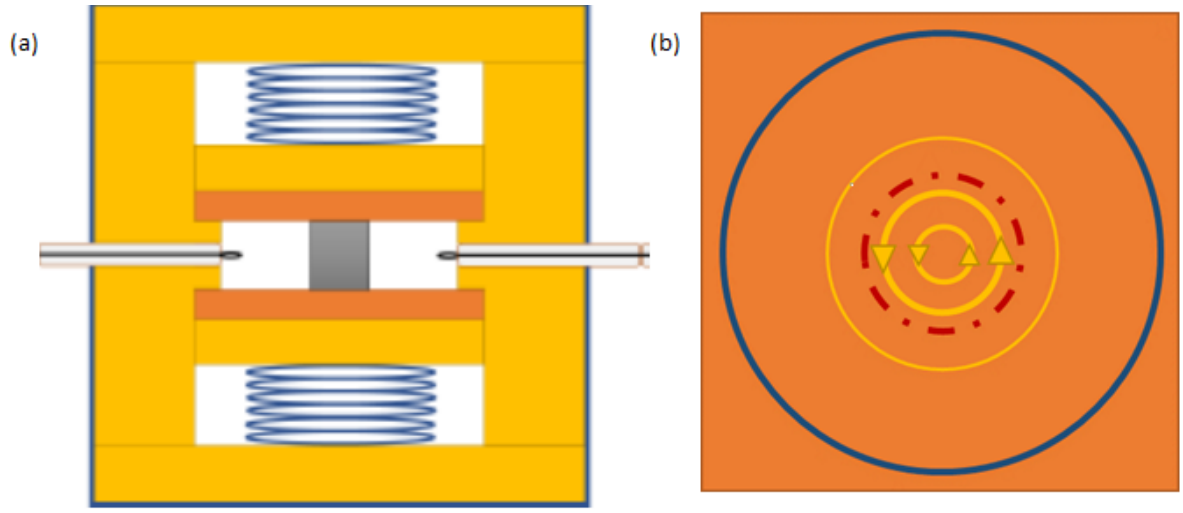

Figure 4. (a) Sketch of the transverse section of the dielectric resonator (DR) for R_s measurements. (b) Current density distribution (yellow circles) inside the cavity (blue circle) on the sample (orange square). The maximum current density is within the dielectric region (red dashed circle) and vanishes exponentially outside of the dielectric.

If an oscillating field is set up within a cavity it will gradually decay because of losses. These losses are mainly due to the finite conductivity of the resonator walls, the losses in the dielectric material within the resonator, and the radiation out of any apertures in the walls. The influence of the absorption on the resonator modes can be characterised by the quality factor Q_0. The unloaded quality factor Q_0 is one of the fundamental parameters in RF and microwave electronics and is proportional to the ratio of stored energy W to the power P dissipated in one

RF cycle. Knowing this, we can formulate the loss equation from which one can derive the relationship between the unloaded quality factor and the surface resistance R_s [32,33]:

$$\frac{1}{Q_0} = \sum_i \frac{R_{s,i}}{G_i} + p\tan(\delta_d). \quad (8)$$

Here, p describes the filling factor which is a dimensionless parameter indicating the ratio of the energy stored in the dielectric to that in the entire resonator , $\tan(\delta_d)$ the loss tangent, and G the geometrical factor, whereas the index i counts the surfaces of the resonator. How the geometrical factor and filling factor can be determined is extensively discussed in [27]. To determine the surface resistance of the samples we can rewrite the equation above, under the assumption that the top and bottom surface (covered by the samples) are the same, and that the lateral-wall losses can be neglected [32] to:

$$R_s = \frac{G}{2}\left(\frac{1}{Q_0} + p\tan(\delta_d)\right). \quad (9)$$

Tests were done at room temperature (RT) and 77 K to determine the behaviour of the laser-treated samples. The cool-down of the DR is achieved by immersing the whole resonator structure into liquid nitrogen. Before the immersion an atmosphere of nitrogen is created by purging the air inside the resonating structure with nitrogen gas. The same procedure is repeated during extraction and warm-up. As the sensitivity of the measurement can suffer due to constant boiling of the liquid nitrogen and possible trapped bubbles in the coupling loops, the measurement was done twice on two different days to assure repeatability and accurate results.

3 RESULTS

3.1 Surface characterisation

Figure 5 shows the low (a), medium (b) and high (c) magnification of planar SEM micrographs of copper samples and stainless steel after laser ablation surface engineered with laser processing parameters shown in Table 1. The SEM micrographs were taken in compositional contrast mode using a backscattered electron detector.

The laser processing for Sample 1 was chosen to be below the ablation threshold which led the surface to go through a rapid melt followed by rapid solidification. A rippled surface is constructed after solidification. The bright contrast represents an oxide surface with patches of dark area which can be related to a more metallic or lower Z material.

All other samples (2, 3, 4 and 5) were irradiated under laser process parameters that yielded surface ablation. This produced shallow grooves with various degrees of nano-particle coverage. By reducing the scan width below the width of beam size (30 μm) the consecutive scans overlap which results in deeper grooves and deeper nanoparticle coverage. This can be clearly seen in the different surface topography evolved between Samples 2 to 4. It has been shown that the reduction in SEY is due to the presence of deep grooves and the nanoparticle location on the surface [20].

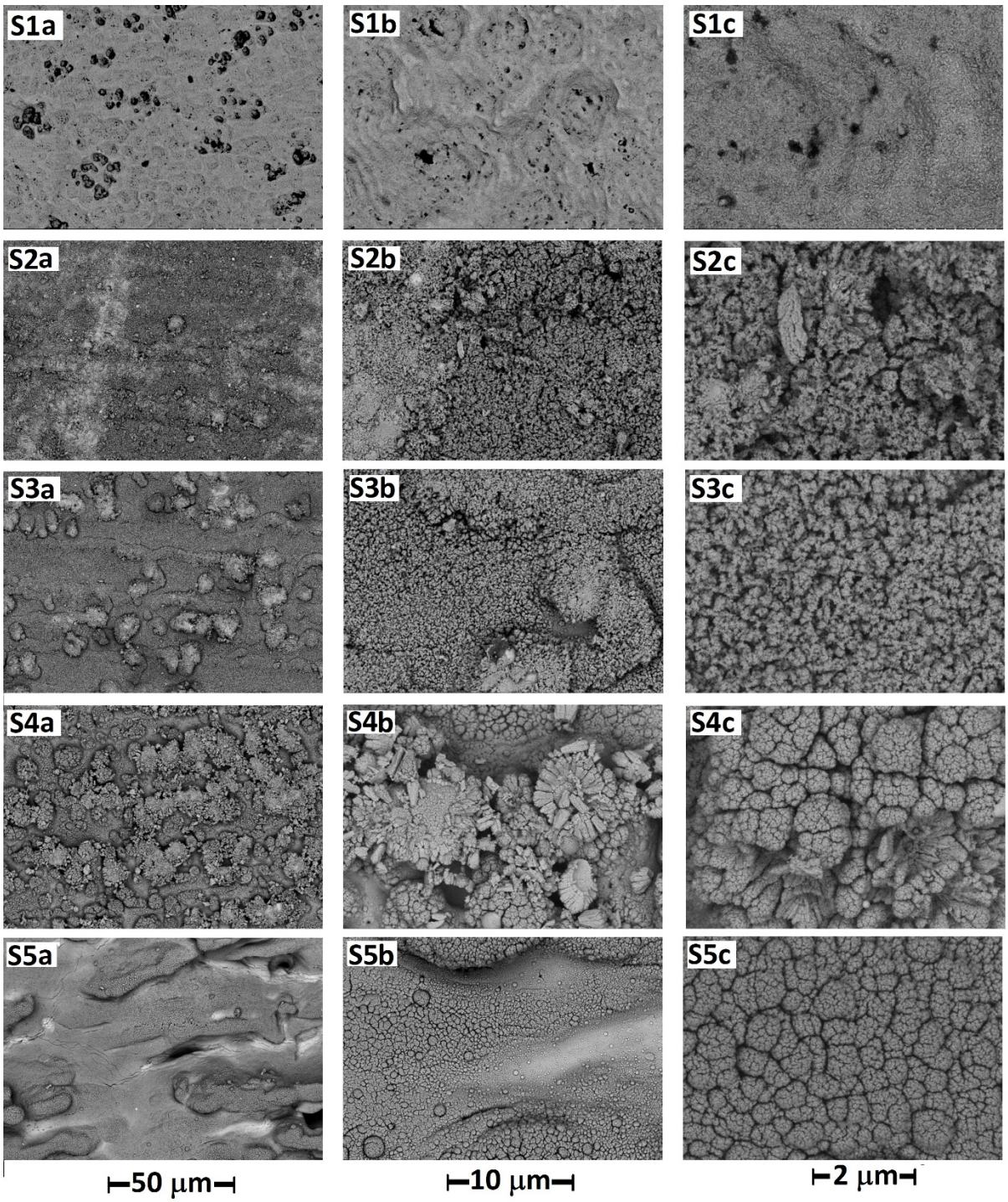

Figure 5. The low (a), medium (b) and high (c) magnification of planar SEM micrographs of copper and stainless steel samples after LASE with laser processing parameters shown in Table 1.

3.2 SEY

Figure 6 depicts the SEY (δ) of the untreated and laser-treated surfaces with various laser processing parameters of copper samples with respect to primary electron energy. The SEY of the untreated sample peaks at E_p = 360 eV for a δ_{max} = 2.1. For primary electron energy E_p >

360 eV the yield δ, gradually decreases and stays at $\delta > 1.3$. Sample 1 showed similar dependency of SEY with respect to primary electron energy but with faster rate of increase for $E_p < 400$ eV, peaking at slightly higher value $\delta_{max} = 2.2$, with 8 to 10% higher value of δ for all primary electron energies. In all the other cases of laser treated samples, the δ increases at a slower rate in comparison to the untreated sample for the primary electron energy $E_p < 600$ eV and stays below $\delta = 1$. It gradually flattens out at $E_p < 1000$ eV and just above and below $\delta = 1$, depending on surface topography.

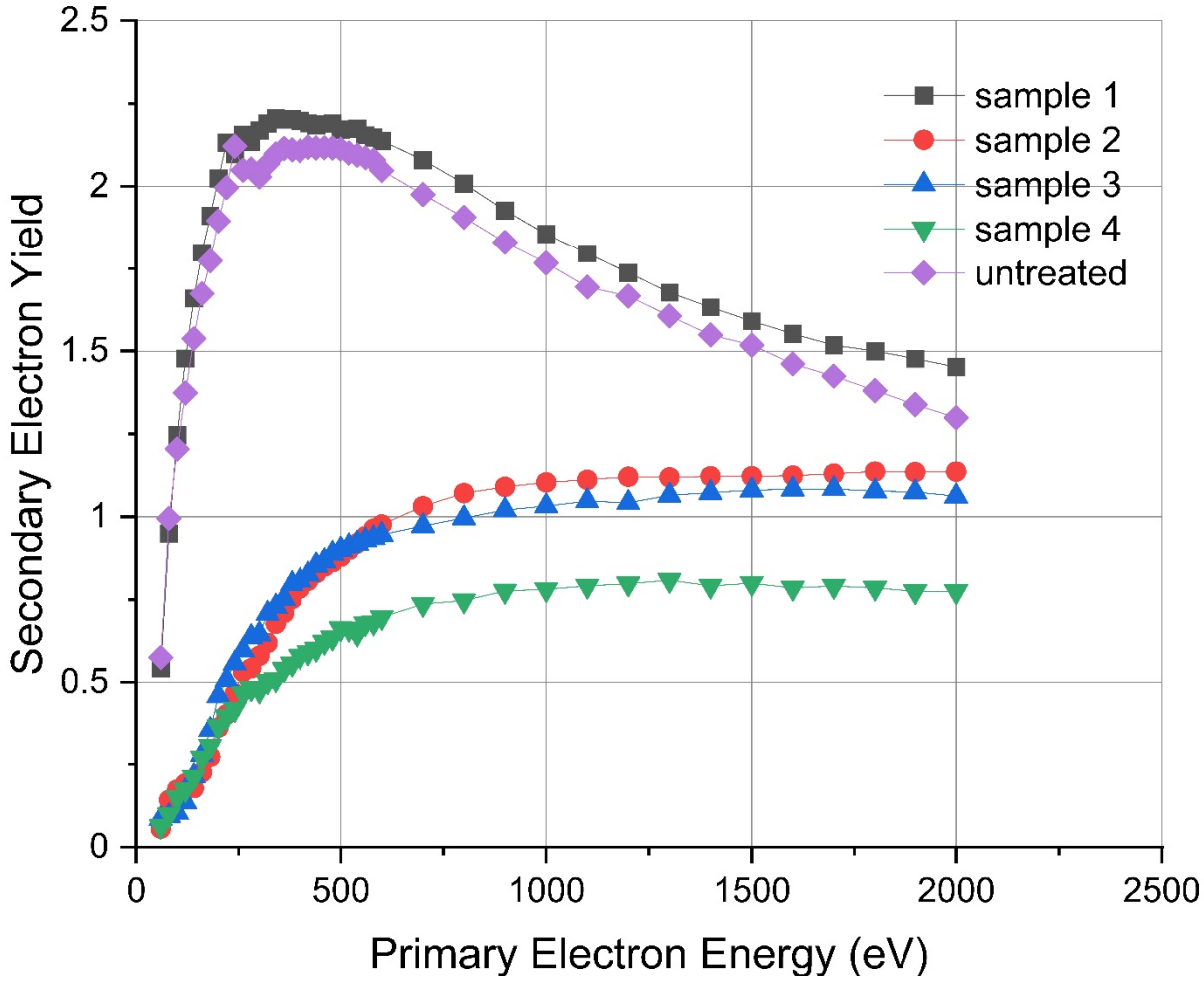

Figure 6. SEY as a function of incident electron energy for the untreated and the laser treated OFHC copper.

Figure 7 depicts the secondary electron yield SEY (δ) of the untreated and laser-treated stainless steel samples with respect to primary electron energy. The trend of the SEY curve follows the same trend as was measured for the copper sample. The SEY of the untreated

sample shows a peak at E_p = 360 eV for a δ_{max} = 2.47. For the laser treated sample, the δ increases at a slower rate in comparison to the untreated sample over the primary electron range E_p < 600 eV and stays below δ = 1.5 It gradually flattens out at E_p < 800 eV.

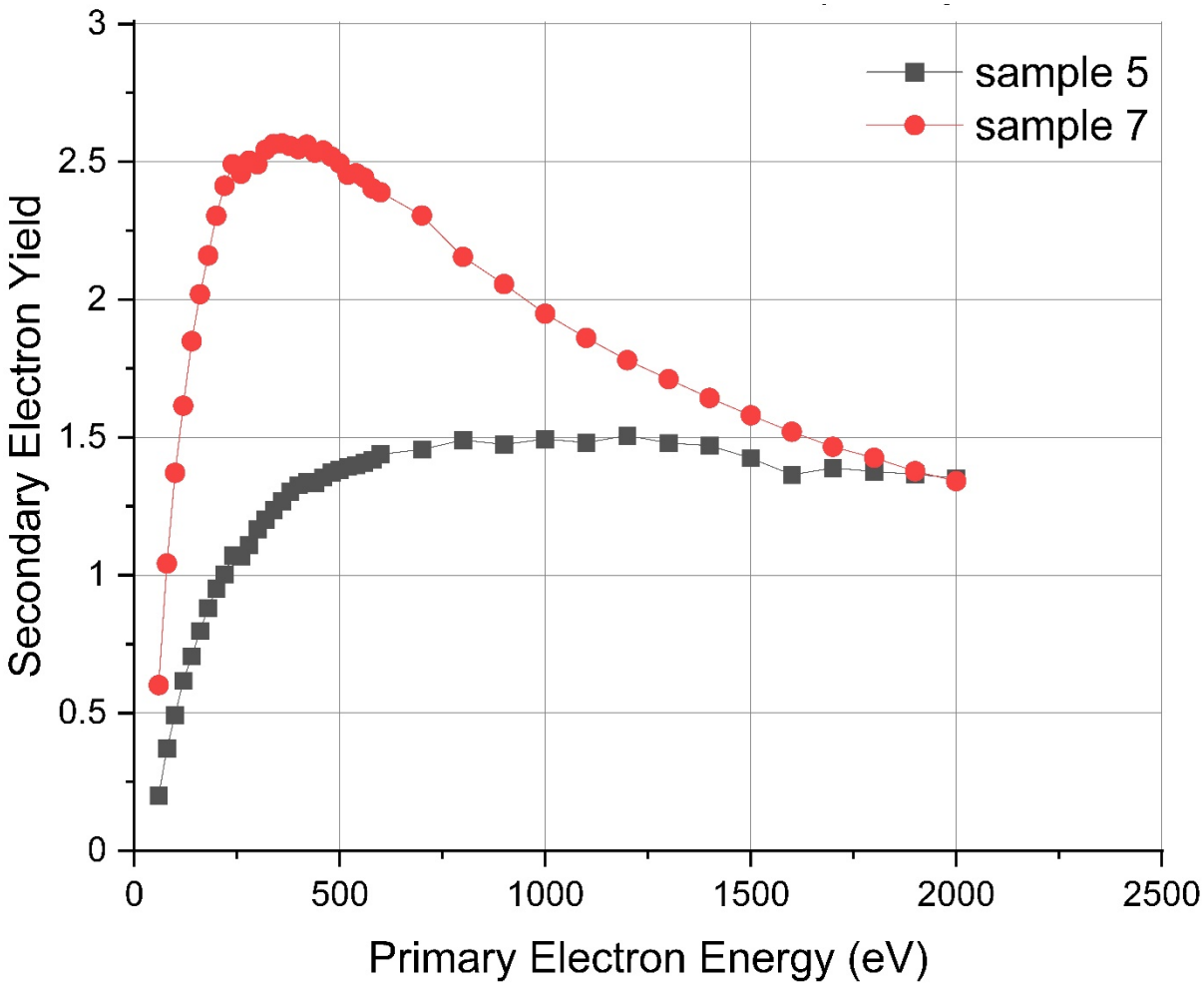

Figure 7. SEY as a function of incident electron energy for the untreated and the laser treated Stainless steel flange.

3.3 Vacuum properties

ESD yields of LASE treated and reference samples as a function of accumulated electron dose for H_2, CH_4, CO and CO_2 are shown in Figure 8.

Untreated copper samples C3 and C4 show identical results, therefore only sample C3 is shown. Both LASE treated samples C1 and C2 have lower ESD than a reference untreated sample C3 for a whole range of electron doses. The ESD yield for Sample C1 are lower than for C2 from initial bombardment up to a dose of approximately 3×10^{23} e^-/m^2, the results are identical for higher doses.

The ESD yields for stainless steel sample SS1 with LASE are comparable with an untreated sample SS2.

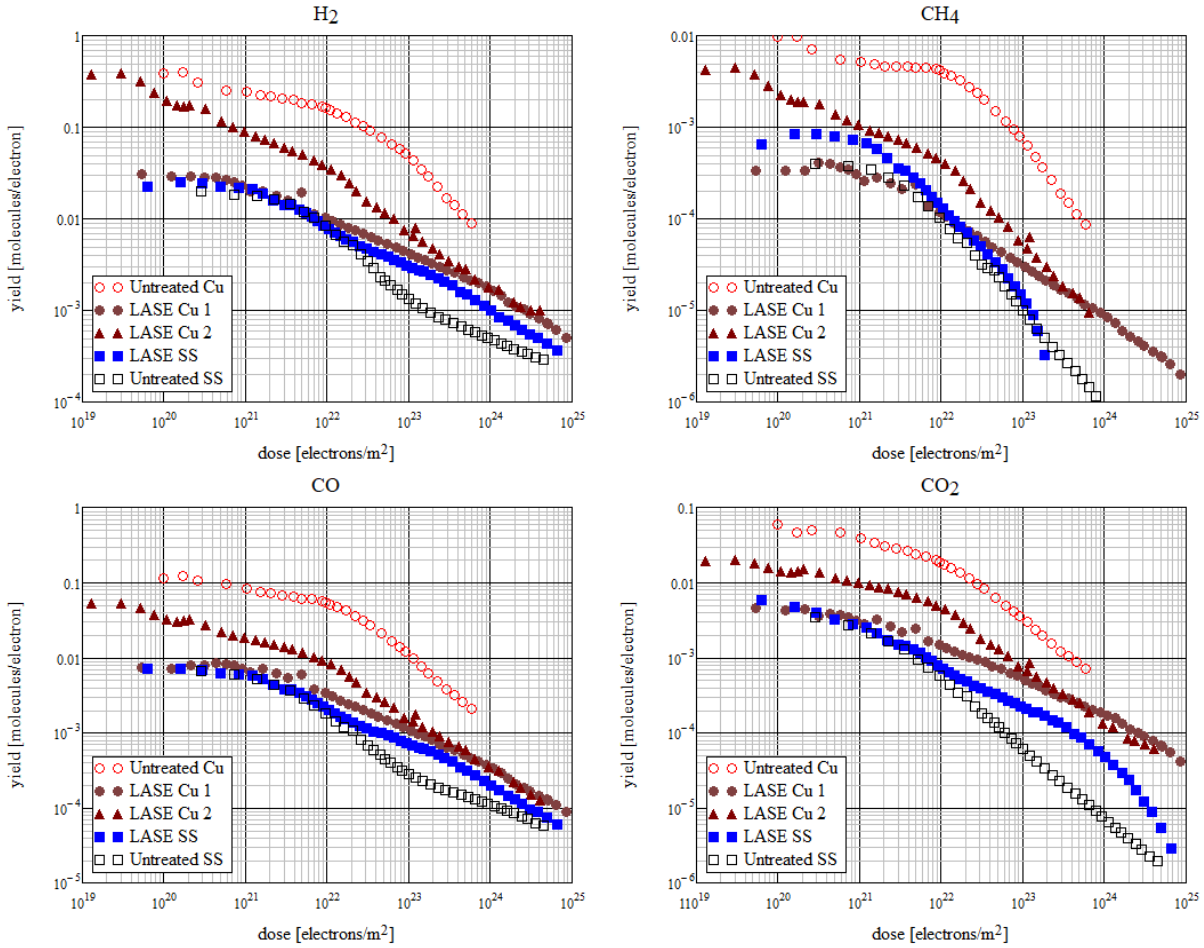

Figure 8. ESD yields of LASE treated and reference samples as a function of accumulated electron dose for different gas species.

3.4 RF surface resistance

The results of the surface resistance measurements performed at room temperature and at 77 K are summarised in Table 2. Two consecutive measurements on two different days were performed and led to similar results within a maximum of 5 % difference. The average value of the results are shown.

Table 2. Surface resistance at RT and 77K. ΔR_s refers to the increment in resistance with respect to the untreated samples.

Samples set	S1 Cu	S5 SS	S2 Cu	S3 Cu	S4 Cu	S6 Cu	S7 SS

Laser parameters	30 W, 0.15ns, 600 kHz, 10 μm	30 W, 0.15ns, 600 kHz, 10 μm	20 W, 2 ns, 60 kHz, 50 μm	20 W, 2 ns, 60 kHz, 10 μm	30 W, 2 ns, 60 kHz, 10 μm	Untreated	Untreated
R_s(RT) [mΩ]	24.6±1.2	288±14	24.9±1.3	28.5±1.4	39.4±2.0	23.4±1.2	243±12
R_s(77K) [mΩ]	10.1±0.5	246±12	9.8±0.5	14.1±0.7	25.3±1.3	10.7±0.54	211±11
ΔR_s(RT) [%]	5	18	6.5	21.8	68	-	
ΔR_s(77K) [%]	-5	16	-10	31.6	136	-	

4 DISCUSSION

The solution to a problem for one part of a particle accelerator should not be a cause of a new problem for another. Thus, LASE as a solution to the BIEM and e-cloud mitigation problem has been examined for possible impact in other parts. The main concern was possible beam loss due to the particulate generation in the beam pipe [34,35,36], increased surface resistance [22,23] and higher outgassing (due to higher physical surface area).

4.1 Development of LASE parameters and impact of LASE on the RF surface resistance

The surface topography induced by LASE depends very much on fluence and number of pulses (or overlap). There is an upper threshold fluence for nanostructure formation. The size of the nano-features increases with increasing number of pulses at a given fluence. Similarly for a fixed number of laser pulses, the feature size can increase with increasing fluence. Thus, the size and shape of nanostructures can be controlled by varying fluence and the number of pulses. Two effects lead to feature size growth with an increasing number of pulses: (1) enhanced energy absorption, and (2) geometric effect. The enhanced absorption of energy is due to previously generated nanoparticles. On the other hand, the geometric effect is caused by the scattered energy due to increased surface roughness. The size of the nanoparticles does not indefinitely increase with number of pulses and fluences. Many of these nano-features turned into microstructures with a sufficient number of pulses and value of fluence. The exact magnitude of the latter two parameters depends on the specific material. Sample 2 and 4 are processed under the same laser parameters (same peak fluence) but at different pitch width. Sample 2 was processed with a beam diameter of 30 μm but at pitch width of 50 μm. No overlapping takes place which can clearly be seen from SEM images (Figure 5-S2a) showing that the scanned lines are well separated. The surface is covered with nano-pores and nano-protrusion as can be seen in Figure 5 (S2c). In contrast the scan lines are not distinguishable due to the overlapping of the scanning beam (Figure 5 (S4a)). Due to multiple scanning the nano-protrusion have turned into micro coral reef feature which covers almost the entire

surface. This surface topography transformation led to a decrease in SEY from $\delta = 1.1$ at E_p = 1000 eV for sample 2 to $\delta = 0.78$ for sample 4. It further increased the surface resistance from 24.9 to 39.4 mΩ (an increase of 58%) at room temperature and from 9.8 to 25.3 mΩ (an increase of 258%) at LN_2 temperature. A comparison between sample 3 and 4 where the pitch distance is kept the same but the fluence per pulse is increased obtained a similar result. The surface topography transformation led to a decrease in SEY from $\delta = 0.97$ at E_p = 1000 eV for sample 3 to $\delta = 0.78$ for sample 4. It further increased the surface resistance from 28.5 to 39.4 mΩ (an increase of 38%) at room temperature and from 14.1 to 25.34 mΩ (an increase of 80%) at LN_2 temperature.

Sample 1 was irradiated with laser parameters below ablation threshold. This led to a smooth rippled surface as seen in Figure 5-S1a and consequently increased the δ_{max} from 2.1 to 2.2. This increase could be as a result of a higher oxidation state of the surface after laser processing in air, a rippled surface or a combination of both.

By comparing all the laser treated surfaces to the as received sample it can be seen that in all cases there is an increase in surface resistance at room temperature. With the exception of sample 1 which was irradiated with laser parameters below ablation threshold, the increase in surface resistance at room temperature correlates with a reduction in SEY, i.e. the larger the surface topography (deep groove or higher volume of nano-particle surface coverage) the lower the SEY and the higher the surface resistance. At room temperature, there is an increase of 6.5, 21.8 and 68% in the surface resistance for sample 2, 3 and 4 respectively.

These results can be compared to our earlier results obtained on copper samples performed with a different type of a resonator operating at 7.8 GHz, see details in Ref. [20]. The untreated copper can be considered as reference. Thus, R_s = 33±7 mΩ measured at 7.8 GHz in Ref. [20] is slightly higher than R_s(S6,RT) = 23.4±1.2 mΩ. Considering that surface resistance increases with frequency proportionally to $\sqrt{f}$, these results are comparable. The LASE treatment in earlier work [20] results in an RF surface resistance increase by a factor between 2.3 and 3.9. However, unexpectedly, the surface resistance at LN_2 temperature behaved differently for samples 1 and 2. In both cases whilst the surface resistance is within the error bars with respect to the untreated samples, there was an increase of 5 and 6.5% respectively in their corresponding room temperature surface resistance. The increase of 31% in surface resistance at LN_2 for sample 3 may still be tolerable taking into account that the SEY is considerably reduced from 2.1 to 1.03. The largest increase of 136% in surface resistance at LN_2 temperature was seen in sample 4 where the SEY reduced considerably to 0.78. The high

increase in surface resistance and low SEY is most probably associated with deep grooves although this is not observable from the surface (Figure 5-S4a). Thus the LASE surface obtained with laser treatment parameters reported in this work for sample S2 change R_s insignificantly (just above the sensitivity level). This result is much better than one previously reported in Ref. [20] and the issues of beam impedance due to an increase of RF surface resistance in particle accelerators is partly mitigated

4.2 Impact of LASE on vacuum properties

Although LASE samples are the same as untreated samples made of the same material, the surface of LASE samples has much greater physical area than that of untreated surfaces. One of the main concerns of vacuum design has been whether the LASE surface would adsorb more gas during treatment and exposure to air and how this impacts on its vacuum properties such as thermal outgassing, photon and electron stimulated desorption, TD, PSD and ESD respectively.

In particle accelerators in general, the inner part of vacuum chambers can be irradiated by synchrotron radiation (SR) with a wide range of energies, from eV to MeV and/or by multipacting electrons (on a range from eV to 1 keV). These photon and electron bombardments are the main source of gas in the beam vacuum chambers of accelerators: PSD and ESD. TD is important mainly for the accelerators with no SR.

It should be noted that in the PSD process, the cross section of direct photon-gas interaction is quite low. The PSD is a two-step process: photons produce photoelectrons and these photoelectrons stimulate the gas desorption at the locations of leaving and arriving at the surface. Thus, the mechanism of gas desorption in both PSD and ESD is similar. Therefore, vacuum properties of different materials and treatment can be compared in the ESD measurements when the ESD yields of one material are lower than the other. The same can be observed in a particle accelerator in the presence of SR and/or electron multipacting.

Both the laser treated copper samples C1 and C2 have ESD yields lower than the untreated samples C3 and C4. Since the results for the untreated samples C3 and C4 are identical, all differences in results for samples C1 and C2 can be associated with the laser treatment. Samples C1 and C2 have been irradiated with energy per pulse of 333 and 500 μJ respectively, which resulted in an SEY of $\delta = 0.78$ and $\delta = 1.01$. It is therefore expected that sample C1 will have much deeper grooves and higher levels of surface topographical defects. This leads to a higher surface areas which can be observed in the SEM micrograph of samples S3 and S4 as depicted in Figure 5. In the whole range of doses the ESD yields for sample C2

are lower than the ones for sample C3 by a factor 2–5 for H_2 and CO_2 and a factor 3–10 for CH_4 and CO. The initial ESD yields for sample C1 are a factor of 3–5 lower than for sample C2 for H_2, CH_4, CO and CO_2. These results are identical for the doses above 3×10^{23} e^-/m^2.

In these experiments the test samples for ESD were grounded during electron bombardment. In this configuration, the true secondary electrons and backscattered electrons from the test sample can have considerable effect if the total yield of the two components are comparable to the primary electron fluence. The secondary electrons will be directed toward the untreated area, which in turn can contribute to the total ESD recorded. Hence, for a laser treated sample under reported experimental condition, which has a reduced SEY (in case of C1 and C2 the SEY reduced by 63% and 51%, respectively), the initial ESD is expected to be lower, as illustrated by our results in Figure 8. However, if the samples were positively biased with respect to the electron gun energy, then the total secondary electrons are suppressed and any deviation between the laser treated and virgin sample will be related to their surface chemistry. In our previous study we have shown [15] that the surface chemistry of the laser treated samples is dependent on the atmosphere they are in during laser ablation. If the LASE is done in air, a fully metal oxide state is stablished with no carbon present. The study [15] further illustrated that long exposure to electron bombardment will result in the build-up of a thick layer of amorphous carbon that will reduce the SEY even further. The gradual drop in ESD level observed for all the samples under electron bombardment and the approaching to a saturated level after bombardment above a dose of $\sim1\times10^{25}$ e^-/m^2 can be explained by the build-up of such a thick film. This in turn will harmonize the surface chemistry which has a substantial effect on the SEY magnitude. In our follow-up studies we will carry out the same procedure but with a biased test sample. This will give the opportunity to quantitatively and qualitatively determine both the effect of surface chemistry and magnitude of SEY on ESD process. Another plausible effect that may also happen and influence the observed results is that during the laser ablation, the gas molecules released and the ablated layer on the copper sample is depleted from the gas molecules. The depletion of sample C1 is therefore greater than the depletion of sample C2. The gas diffusion from deeper layers slowly diminishes this difference, hence the C1 and C2 results are identical for the doses above 3×10^{23} e^-/m^2. In addition, the trend of untreated sample C3 shows that if bombardment continues for larger doses, it will become the same as for sample C1 at the dose $\sim1\times10^{25}$ e^-/m^2. It can be concluded that the laser treatment with these applied laser parameters can significantly (up to a factor ~10) reduce initial ESD yields. However this benefit reduces with dose.

It has been shown that the ESD yields for treated and untreated stainless steel samples SS1 and SS2 are quite similar. In the case of stainless steel, the SEY of laser treated sample SS1 was reduced by 40% which according to the hypothesis above should have reduced the ESD in comparison to the untreated stainless steel. However the ESD for the whole range of dose are very similar. Earlier study [15] showed, in contrast to the copper, the surface chemistry of the laser treated stainless steel sample in air atmosphere and argon remained the same which was the same as the untreated stainless steel sample. Another explanation may be that in the case of copper samples, the sample material used for ESD and SEY were of the same copper composition whereas for the stainless steel, the reported SEY and EDS samples are not exactly of the same grade. This may have produced a different topography and hence SEY although the same parameters of laser processing were employed. Based on the current finding, it can only be concluded that the laser treatment with these applied laser parameters does not affect vacuum properties of stainless steel.

In order to qualitatively and quantitatively determine the dependence of ESD on the SEY, the SEY of each individual ESD sample should be determined as part of follow-up studies.

5 CONCLUSION

This paper reports on the findings that Laser Ablation Surface Engineering (LASE) treated copper and stainless steel surfaces can be produced to simultaneously meet the three main requirements of any particle accelerator vacuum chamber. Namely, to reduce SEY ≤ 1, to keep the RF surface resistance comparable to an untreated surface and to avoid an increase in gas desorption.

It has been shown that LASE is very effective in producing surfaces with the lowest SEY reported to date. In comparison with existing techniques, these are relatively easy to achieve, reasonably scalable (since the technology already exists for other sectors) and can be easily adapted. The process can be very cost-effective, particularly with the availability of new more powerful and low-cost lasers.

The results in this paper have shown that it is possible to reduce the SEY to ~1 whilst only increasing the surface resistance by 6.5% at room temperature and unchanged at 77K. However, the lower the SEY the larger the increase in surface resistance.

LASE can be easily applied and many parameters readily adjusted resulting in a wide variety of possible structures. Hence it opens up the possibility for producing surfaces with low SEY and acceptable surface resistances.

Further utilisation of the LASE technique is not detrimental to the vacuum properties of the material and in some cases, such as ESD, can be improved. In addition:

- Copper samples treated with LASE have demonstrated lower ESD yields than untreated samples. LASE treatment can significantly (up to a factor ~10) reduce initial ESD yields but this benefit reduces with dose.
- ESD for 316LN stainless steel with LASE is comparable with an untreated sample.

In the application to the particle accelerators, it has been demonstrated that the LASE treatment procedures reported in this paper mitigates the BIEM and e-cloud problem without any deterioration in other properties. Furthermore, the treatment does not increase, and can even improve, vacuum properties and provides surface resistance comparable to that of untreated surfaces.

ACKNOWLEGMENTS

With this paper the Authors thanks Prof. John S. Colligon for his great work as Editor in Vacuum, as a nice colleague and as a good friend. This work was conducted under the aegis of the Science & Technology Facility Council (STFC). The authors would also like to acknowledge the support provided by CERN through funding FCC-GOV-CC-0073/ 1724666/KE3359. UPC funding was provided through the Unit of Excellence María de Maeztu MDM2016-0600.

REFERENCES:

[1] G. Rumolo, G. Arduini, V. Baglin, H. Bartosik, N. Biancacci, et al. Electron cloud observations in LHC. Proc. of IPAC2011, San Sebastián, Spain (2011) p. 2862
[2] J. A. Crittenden, J. V. Conway, G. Dugan, M.A. Palmer, D.L. Rubin, K. Harkay, L. Boon, M.A. Furman, S. Guiducci, M.T.F. Pivi and L. Wang. Investigation into electron cloud effects in the ILC damping ring design. Proc. of IPAC-2012, New Orleans, Louisiana, USA, p. 1963 (2012).
[3] S. Kato, M. Nishiwaki. e-Cloud Activity of DLC and TiN Coated Chambers at KEKB Positron Ring. Proc. of Ecloud'10, Ithaca, New York, USA (2010), p. 37.
[4] D. Alesini, T. Demma, A. Drago, A. Gallo, S. Guiducci, C. Milardi, P. Raimondi, M. Zobov, S. De Santis, T. Demma, P. Raimondi. Experimental measurements of e- -2012, New Orleans, Louisiana, USA, p.1107 (2012).
[5] W. Fischer, U. Iriso. Bunch patterns and pressure rise in RHIC. Proc. of EPAC'04, Lucerne, Switzerland, July 2004, p. 914.
[6] F. Zimmermann. Review of single bunch instabilities driven by an electron cloud. Phys.Rev.ST Accel. Beams **7**, 124801 (2004).
[7] F. Zimmermann. Electron-cloud effects in past & future machines – walk through 50 years of electron-cloud studies. Conf. Proc. C **1206051**, 9-17 (2013). doi: 10.5170/CERN-2013-002.9

[8] V. Baglin and O.B. Malyshev. Beam-induced electron multipacting, electron cloud and vacuum design, Chapter 8 in "Vacuum in Particle Accelerators: Modelling, Design and Operation of Beam Vacuum" ed. by O.B. Malyshev. Wiley VCH (2019).
[9] High-Luminosity Large Hadron Collider (HL-LHC) : Technical Design Report V. 0.1, CERN-2017-007-M, doi 10.23731/CYRM-2017-004
[10] H. Fukuma. Electron Cloud Observations and Predictions at KEKB, PEP-II and SuperB Factories. Proc. Of Ecloud'12, 5-9 Jun 2012, La Biodola, Isola d'Elba, Italy, p. 27 (2012).
[11] G. Stupakov and M. Pivi. Suppression of the effective SEY for a grooved metal surface, Proc. of ECLOUD'04, Napa, California, 19-23 April 2004, p.139 (2004).
[12] P. He, H.C. Hseuh, M. Mapes, R. Todd and D. Weiss. Development of titanium nitride coating for SNS ring vacuumchambers. Proc. PAC01, p.2159 (2001).
[13] W W. Fischer, M. Blaskiewicz, J. M. Brennan, H. Huang, H.-C. Hseuh, V. Ptitsyn, T. Roser, P. Thieberger, D. Trbojevic, J. Wei, S. Y. Zhang, and U. Iriso. Electron cloud observations and cures in the Relativistic Heavy Ion Collider. Phys. Rev. ST Accel. Beams **11**, 041002 (2008).
[14] C. Yin Vallgren, G Arduini, J.Bauche, S. Calatroni, P. Chiggiato, K. Cornelis, P. Costa Pinto, E. Metral, G. Rumolo, E. Shaposhnikova, M. Taborelli, G. Vandoni. Amorphus carbon coatings for mitigation of electron cloud in the CERN SPS. Proc. IPAC'10, Kyoto, Japan, paper TUPD048, p. 2033 (2010).
[15] S. Wang. PhD Thesis. Loughborough University, UK, July 2016.
[16] I. Montero, L. Aguilera, M.E. Dávila, et al. Novel types of anti-ecloud surfaces. In proc. of E-CLOUD12 workshop, ELBA, Italy, 2012, p. 153.
[17] R. Valizadeh, O.B. Malyshev, S. Wang, S.A. Zolotovskaya, W.A. Gillespie and A. Abdolvand. Low secondary electron yield engineered surface for electron cloud mitigation. Appl. Phys. Lett. **105**, 231605 (2014).
[18] R. Valizadeh, O. Malyshev. Apparatus and methods relating to reduced photoelectron yield and/or secondary electron yield. Patent publication number WO2015189645 A1. 17th Dec 2015.
[19] R. Valizadeh, O.B. Malyshev, S. Wang, T. Sian, M. D. Cropper and N. Sykes. Reduction of Secondary Electron Yield for E-cloud Mitigation by Laser Ablation Surface Engineering. Appl. Surf. Sci. **404,** 370–379 (2017). doi.org/10.1016/j.apsusc.2017.02.013.
[20] R. Valizadeh, O.B. Malyshev, S. Wang, T. Sian, L. Gurran, *et al*. Low secondary electron yield of laser treated surfaces of copper, aluminium and stainless steel. Proc. of IPAC 2016, Busan, Korea, 2016, p.1089.
[21] M. Birnbaum, Semiconductor surface damage produced by ruby lasers, J. Appl. Phys. **36**, 3688 (1965).
[22] M. Zobov. Stability limits with Landau damping in the FCC-hh. JINST (to be on-line in a few days)
[23] Sergey Arsenyev, Alexej Grudiev, Daniel Schulte. FCC beam screen impedance. ALERT 2019.
[24] E. Belli, P. Costa Pinto, *et al*. Electron cloud buildup and impedance effects on beam dynamics in the Future Circular e+e– Collider and experimental characterization of thin TiZrV vacuum chamber coatings. Phys. Rev. Accel. Beams **21**, 111002 (2018).
[25] A. Passarelli, C. Koral, M.R. Masullo, *et al*. Sub-THz Waveguide Spectroscopy of Coating Materials for Particle Accelerators. Condens. Matter **5**, 9 (2020).
[26] S. Calatroni, E. Garcia-Tabares Valdivieso, H. Neupert, V. Nistor A. Perez Fontenla, *et al*. First accelerator test of vacuum components with laser-engineered surfaces for electron-cloud mitigation. Phys. Rev. Accel. Beams **20**, 113201 (2017).
[27] FCC-hh: The Hadron Collider. Future Circular Collider Conceptual Design Report Volume 3. Ed. by M. Benedikt et al. Eur. Phys. J. ST. **228**, 755-1107 (2019). https://doi.org/10.1140/epjst/e2019-900087-0.
[28] O.B. Malyshev and K.J. Middleman. In situ UHV RGA "callibration". J. Vac. Sci. Technol. A **26**, 1474-1479 (2008).
[29] P. Krkotic, A. Aguasca and J.M. O'Callaghan. Small Footprint Evaluation of Metal Coatings for Additive Manufacturing. Conference Paper, European Microwave Week 2018, Madrid, 2018.
[30] D. Arcos. Contactless Electrical Resistance of 2D Materials Using a Rutile Resonator. Physica status solidi (b), Volume **256**, Issue 12, (2019).
[31] T. Puig. Coated conductor technology for the beam screen chamber of future high energy circular colliders. Superconductor Science and Technology, 2019.
[32] D. Kajfez and P. Guillon. Dielectric Resonators. Artech House, Inc. 1986.
[33] Z.-Y. Shen et al. High TC Superconductor-Sapphire Microwave Resonator with Extremely High Q-Values up to 90 K. IEEE Transactions on Microwave Theory and Techniques, vol. **40**, no. 12, Dec. 1992.
[34] A. Ferrari, B Goddard, E.B. Holzerm, *et al*. UFOs in the LHC: Observations, Studies and Extrapolations. IPAC-2012-THPPP086, Conf. Proc. C **1205201**, 3936-3938 (2012).
[35] T. Baer, M.J. Barnes, F. Cerutti, *et al*. UFOs in the LHC: observations, studies and extrapolations. Proc. of IPAC2012, New Orleans, Louisiana, USA, (2012), THPPP086.
[36] B. Lindstrom, A. Apollonio, P. Belanger, *et al*. Results of UFO dynamics studies with beam in the LHC. IOP Conf. Series: Journal of Physics: Conf. Series **1067**, 022001 (2018).